

Structural and Statistical Audio Texture Knowledge Distillation for Environmental Sound Classification

Jarin Ritu, Amirmohammad Mohammadi, Davelle Carreiro, Alexandra Van Dine, and Joshua Peebles

Abstract—While knowledge distillation has shown success in various audio tasks, its application to environmental sound classification often overlooks essential low-level audio texture features needed to capture local patterns in complex acoustic environments. To address this gap, the Structural and Statistical Audio Texture Knowledge Distillation (SSATKD) framework is proposed, which combines high-level contextual information with low-level structural and statistical audio textures extracted from intermediate layers. To evaluate its generalizability to a broad range of applications, SSATKD is tested on four diverse datasets within the environmental sound classification domain, namely two passive sonar datasets: DeepShip and Vessel Type Underwater Acoustic Data (VTUAD) and two general environmental sound datasets: Environmental Sound Classification 50 (ESC-50) and UrbanSound8K. Two teacher adaptation strategies are explored: classifier-head-only adaptation and full fine-tuning. The framework is further evaluated using various convolutional and transformer-based teacher models. Experimental results demonstrate consistent accuracy improvements across all datasets and settings, confirming the effectiveness and robustness of SSATKD in real-world sound classification tasks.¹

Index Terms—Knowledge Distillation, Sound Classification, Audio Texture

I. INTRODUCTION

CLASSIFYING real-world audio signals plays a vital role in various applications, ranging from urban scene analysis to marine monitoring [1], [2]. Environmental sound classification (ESC) solutions help to classify signals relevant to these applications and encompass a wide range of tasks involving acoustic event detection in both terrestrial and underwater settings. Well-studied ESC tasks involve recognizing sounds like vehicle horns, animal vocalizations, or human activities in terrestrial, often cluttered, environments [3]. Another

Manuscript received Month XX, 202X; revised Month XX, 202X.

Jarin Ritu, Amirmohammad Mohammadi, and Joshua Peebles are with the Department of Electrical and Computer Engineering, Texas A&M University, College Station, TX, USA (e-mail: jarin.ritu@tamu.edu; amir.m@tamu.edu; jpeebles@tamu.edu).

Davelle Carreiro and Alexandra Van Dine are with the Massachusetts Institute of Technology Lincoln Laboratory, Lexington, MA, USA (e-mail: davelle.carreiro@ll.mit.edu; alexandra.vandine@ll.mit.edu).

DISTRIBUTION STATEMENT A. Approved for public release. Distribution is unlimited. This material is based upon work supported by the Under Secretary of Defense for Research and Engineering under Air Force Contract No. FA8702-15-D-0001 or FA8702-25-D-B002. Any opinions, findings, conclusions or recommendations expressed in this material are those of the author(s) and do not necessarily reflect the views of the Under Secretary of Defense for Research and Engineering. © 2025 Massachusetts Institute of Technology. Delivered to the U.S. Government with Unlimited Rights, as defined in DFARS Part 252.227-7013 or 7014 (Feb 2014). Notwithstanding any copyright notice, U.S. Government rights in this work are defined by DFARS 252.227-7013 or DFARS 252.227-7014 as detailed above. Use of this work other than as specifically authorized by the U.S. Government may violate any copyrights that exist in this work.

¹https://github.com/Advanced-Vision-and-Learning-Lab/SSATKD_Lightning

application of ESC involves sonar signal classification, which seeks to identify underwater sound sources such as vessels and marine life by their acoustic signatures [4], [5]. Sonar signal classification is a key construct in marine biology, defense, and underwater infrastructure monitoring applications.

While there are two modalities of sonar sensing, namely active and passive, this effort focuses on passive sonar, which uses sound waves to assess acoustic signals of interest without active emission of signals. Passive sonar classification presents unique challenges due to the complexities of underwater environments, including low signal-to-noise ratios (SNRs), high variability in acoustic signatures [4], [5], and signal distortion from propagation conditions [6]. Despite differences in setting, both terrestrial and underwater environmental sound classification tasks share common challenges such as low SNRs, high variability in acoustic patterns, overlapping sources, and complex temporal structures [4]–[7]. Traditional signal processing techniques, such as low-frequency analyzer and recorder (LOFAR) spectra [8] and detection of modulation on noise (DEMON) analysis [9], often struggle to distinguish signals of interest in these conditions [4]. To address this, researchers have increasingly turned to machine learning methods like ensemble learning, where multiple models are combined to improve accuracy [10].

While effective, ensemble models are often computationally expensive [11], prompting interest in more efficient alternatives such as pruning [12], quantization [13], and knowledge distillation (KD) [10]. KD compresses deep networks by using soft probabilities (logits) from a large teacher model to guide a smaller student model [14]. These soft labels provide richer supervision than hard labels, helping the student network learn more effectively. This process enables the student to match the teacher’s performance while using fewer resources, making it suitable for deployment on real-time or resource-constrained devices [14], [15]. KD has shown success in computer vision [16] and language processing (NLP) [17], but its use in real-world audio classification, particularly in ESC, remains limited.

Existing KD methods typically emphasize high-level semantic knowledge transfer [18], [19] but often overlook low-level texture features in intermediate audio representations. These features are essential for capturing local acoustic patterns, such as harmonic structure, noise texture, and modulation characteristics. This limitation is especially pronounced in ESC tasks, where texture-based cues may often play a vital role in fine-grained classification [20]. To address this, we propose Structural and Statistical Audio Texture Knowledge Distillation (SSATKD), a novel distillation framework that enables student models to learn not only final predictions but

also rich audio texture representations from their teachers. SSATKD integrates two specialized modules: one for capturing structural texture patterns and another for quantifying statistical texture variations.

Overall, the contributions of this work are as follows:

- In-depth analysis of different knowledge distillation strategies (*e.g.*, teacher-student architectures, loss functions) across four diverse datasets within the environmental sound classification domain
- Incorporation of a novel Edge Detection Module for extracting structural texture
- Implementation of 2D Earth Mover’s Distance (EMD) loss to quantify differences in statistical textures

II. RELATED WORK

A. Audio Texture Representation

In audio data analysis, parallels can be drawn between sound and visual textures [21] which can be categorized into structural and statistical aspects [22]. In 1D audio waveforms, time represents the temporal dimension, and amplitude reflects the intensity of the sound at each time point [23]. Temporal dependency in audio signals mirrors the spatial dependency observed in 2D images, wherein neighboring pixels exhibit spatial relationships [23]. The repetitive patterns or rhythms in audio signals correspond to structural textures in images, revealing regularity and patterns in the sound. These structural textures capture the arrangement of elements within the signal, providing insights into recurring patterns present in the audio data. Meanwhile, amplitude variations in audio signals reflect statistical textures, similar to the intensity values observed in images [24]. These statistical textures encapsulate information about the distribution and variability of signal amplitudes, offering insight into the distribution and characteristics of the audio signal [23].

Recent efforts have explored audio classification algorithms by treating time-frequency representations of audio signals as images, a concept inspired by biologically motivated work on object recognition [25], [26]. By drawing parallels between the characteristics of images and 2D time-frequency representations, methods such as Gabor filters and wavelet transforms can extract meaningful texture information from the data [27], [28]. These textures are simpler and more consistent than complex sounds like speech or music, motivating the need for improved sound recognition and auditory representation in acoustic data [29].

B. Deep Learning Methods

Recent advancements in acoustic signal classification have leveraged deep learning to automatically extract features from time-frequency representations such as spectrograms, mel-frequency cepstral coefficients (MFCCs), and log-mel spectrograms. These representations are widely used to identify a diverse range of acoustic events of interest. Numerous benchmark datasets, such as UrbanSound8K [30] and ESC-50 [3] have driven progress in the field by providing labeled audio clips across different environmental scenarios. Models based

on convolutional neural networks (CNNs) have demonstrated strong performance in ESC tasks due to their ability to capture local spectral patterns [31], while attention mechanisms and transformer architectures have recently been introduced to improve robustness and contextual understanding in complex acoustic scenes [32], [33].

Similarly, passive sonar processing applies traditional techniques like LOFAR and DEMON to convert raw underwater acoustic data into spectrograms or cepstral features, which are then fed into neural networks [7], [27]. Deep neural networks (DNNs) have been effective in modeling both spatial and temporal patterns within these time-frequency inputs [34]. Recurrent architectures like long short-term memory (LSTM) networks and hybrid CNN-LSTM combinations further enhance performance by capturing long-term dependencies, which are essential for both temporally evolving sound events in environmental scenes [35] and sequential ship noise in passive sonar [36], [37]. However, all of these methods can be computationally expensive and often require large datasets, limiting their application in real-time or resource-constrained environments.

C. Knowledge Distillation Vs Transfer Learning

Transfer learning is a widely used strategy in machine learning, particularly when training data is limited or difficult to collect [38], [39]. Further, transfer learning has been widely used in audio tasks, such as sound event tagging [40], emotional audio research [38], [41], and environmental audio event detection using semi-supervised learning [42]. In these scenarios, pre-trained models from related domains are used to improve performance on new tasks, leveraging the knowledge learned from the source domain. Similarly, ESC methods can suffer mismatches between the source and target domains due to different recording conditions or frequency characteristics that can limit the effectiveness of transfer learning [43], [44]. Transfer learning can be even less effective in domains like passive sonar, where acoustic properties differ significantly from general audio data. Underwater signals often exhibit high variability due to factors such as vessel movement, environmental noise, and propagation effects related to salinity, depth, and temperature [45].

Models pre-trained on unrelated domains (*e.g.*, speech) may fail to generalize well to sonar signals, leading to suboptimal performance [38], [42], [46]. Knowledge distillation offers an alternative strategy by compressing task-specific knowledge from a large teacher model into a smaller, efficient student model [47]. Unlike transfer learning, which often retains the original model size and domain, knowledge distillation enables lightweight models to approximate the performance of larger ones on the same task. It has been applied in a wide range of tasks, including computer vision, speech recognition, and increasingly, audio classification [19], [41], [48]. Knowledge distillation has demonstrated the ability to preserve task-specific performance while significantly reducing computational overhead, making it particularly well-suited for real-time applications in resource-constrained environments.

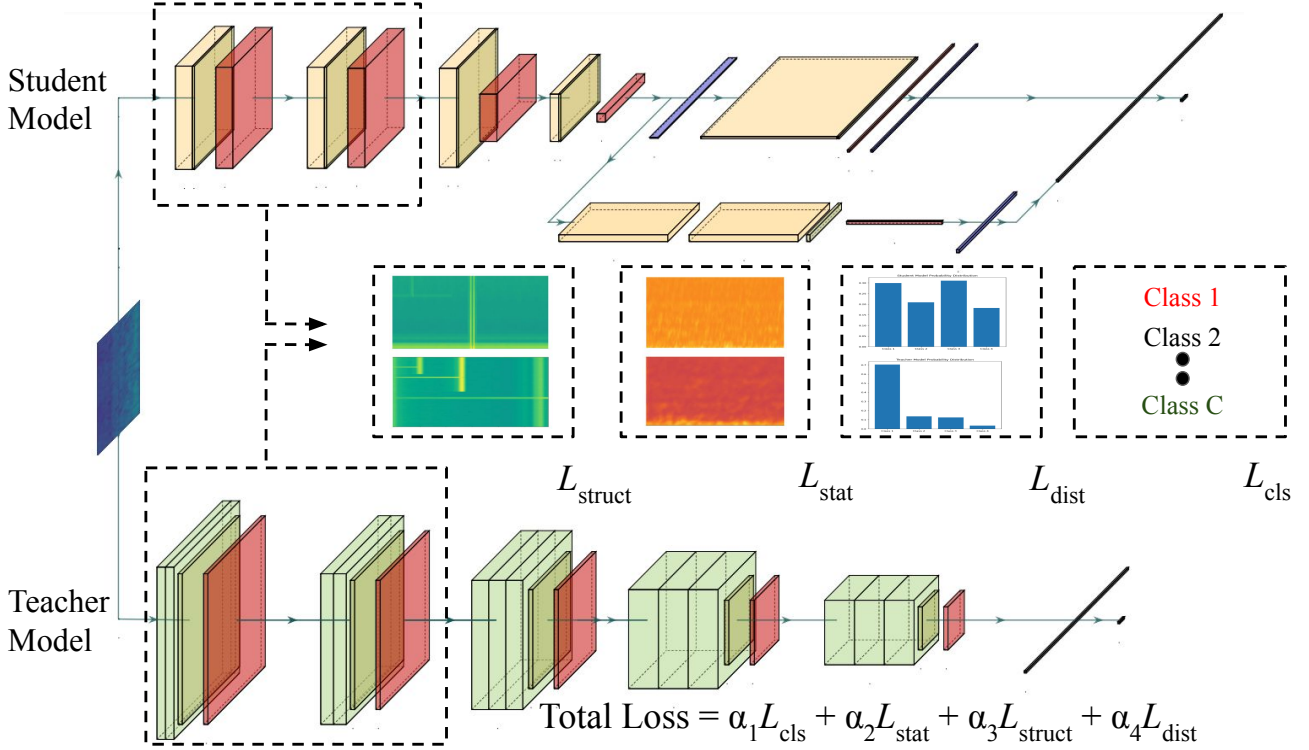


Fig. 1: Overview of the proposed SSATKD framework. The upper network represents the student model, a Histogram Layer Time Delay Neural Network (HLTDNN) adopted from the original HLTDNN paper [39]. The framework is designed to be flexible, accommodating any combination of student and teacher models. In this work, the student model is fixed as the HLTDNN, with the teacher model presented as a general structure that can be any of the following pre-trained audio neural network (PANN) model architectures: CNN14, ResNet38, MobileNetV1, or transformer-based foundation models: Wav2Vec 2.0, HuBERT, and Whisper. For CNN-based teachers, each convolutional block includes activation and pooling. Yellow and green blocks represent student and teacher layers, respectively. For transformer-based teachers, features are extracted from early encoder layers and aligned with the student for texture-based distillation. In addition to response-based knowledge distillation, SSATKD incorporates feature-based distillation by extracting texture knowledge from low-level features. Specifically, statistical and structural textures are extracted after the second layer of both the teacher and student models. The total loss is calculated as a weighted sum of classification, statistical, structural, and distillation losses.

III. METHODOLOGY

The proposed SSATKD framework is illustrated in Figure 1. Initially, the input signals are transformed into time-frequency representations, which are then passed into the SSATKD network. The framework focuses on extracting both structural and statistical texture features from the first two layers of the teacher and student models, leveraging the fact that early layers of neural networks capture distinct texture information [49]. Following the distillation approach from [10], the teacher and student networks are aligned by minimizing a combination of response-based and feature-based losses. This alignment ensures the student model effectively learns both high-level semantic information and low-level texture details from the teacher. For statistical texture module, building upon previous research by Zhu et al. [50], the quantization and count operator (QCO) methodology is refined by replacing their linear binning function with radial basis functions (RBFs) for smoother quantization [51]. For the structural texture module, a novel Edge Detection Module is introduced, combining hierarchical decomposition techniques, including the Laplacian Pyramid

(LP) and edge detection filters.

A. Statistical Texture Module

Statistical textures are first extracted by applying Global Average Pooling (GAP) to the input feature matrix $\mathbf{A} \in \mathbb{R}^{C \times H \times W}$, where H and W represent the height and width of the feature map, and C is the number of channels. This operation results in a global averaged feature vector $\mathbf{g} \in \mathbb{R}^{C \times 1 \times 1}$, which aggregates information across all spatial dimensions, providing a compact representation of the original feature matrix. Next, the cosine similarity between each spatial position \mathbf{A}_{ij} (where $i \in [1, W]$ and $j \in [1, H]$) in the feature map \mathbf{A} and the global averaged feature vector \mathbf{g} is computed, resulting in similarity features \mathbf{S} with dimensions $1 \times H \times W$. \mathbf{S} is then reshaped to $\mathbf{S} \in \mathbb{R}^{H \times W}$ and quantized into Q levels, denoted as $\mathbf{Q} = [Q_1, Q_2, \dots, Q_N]$. The n -th quantization level Q_n is defined in Equation 1:

$$\mathbf{Q}_n = \frac{n}{N} (\max(\mathbf{S}) - \min(\mathbf{S})) + \min(\mathbf{S}), \quad (1)$$

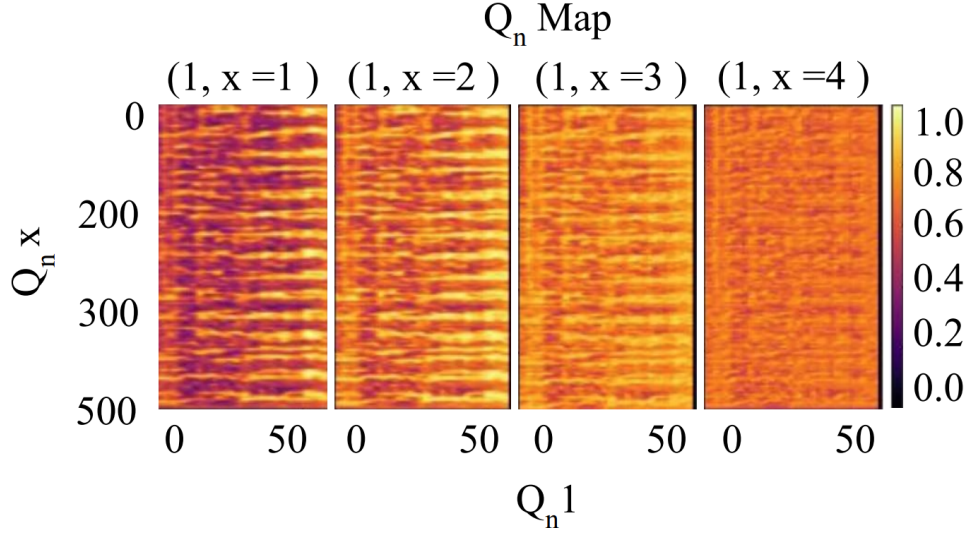


Fig. 2: Visualization of 4 co-occurrence matrices out of the 16 possible matrices, corresponding to a 4-level quantization process. Each matrix captures the pairwise quantization co-occurrence between adjacent spectrogram values in the feature maps. The color intensity represents the frequency of co-occurrence for each pair of quantized levels. Brighter regions (yellow to light green) indicate stronger co-occurrences, while darker regions (dark blue and purple) suggest sparse co-occurrences.

where N is a hyperparameter for the maximum number of quantization levels, and $n \in \{1, 2, \dots, N\}$. To enhance the encoding process by capturing a smoother gradient compared to the linear basis function used in [50], the similarity values are further quantized into $\mathbf{E}_i \in \mathbb{R}^N$ using an RBF. Here, i ranges from 1 to HW , and each dimension $n \in \{1, 2, \dots, N\}$ of \mathbf{E}_i is calculated using Equation 2. This quantization process is centered around predefined levels and controlled by the bandwidth parameter γ , set to $\frac{1}{N/2}$.

This choice of γ ensures effective coverage of the interval between the selected centers \mathbf{Q} :

$$\mathbf{E}_{i,j} = \exp\left(-\gamma^2 (\mathbf{Q}_n - \mathbf{S}_i)^2\right) \quad (2)$$

The quantized tensor \mathbf{E} is then reshaped into $\mathbb{R}^{N \times 1 \times H \times W}$. For each pair of adjacent spectrogram spectrogram values in the feature map, $\mathbf{E}_{i,j} \in \mathbb{R}^{N \times 1}$ and $\mathbf{E}_{i,j+1} \in \mathbb{R}^{N \times 1}$, their outer product $\hat{\mathbf{E}}_{i,j}$ is computed to capture adjacent information, as defined in Equation 3:

$$\hat{\mathbf{E}}_{i,j} = \mathbf{E}_{i,j} \times \mathbf{E}_{i,j+1}^T \quad (3)$$

Here, T denotes the matrix transpose, and \times represents matrix multiplication. The resulting co-occurrence matrices for adjacent spectrogram cell pairs are visualized in Figure 2, showing how neighboring spectrogram values are correlated. The color scale in the figure ranges from dark purple (representing lower values) to bright yellow (representing higher values). The increasing brightness from the left to right images indicates stronger correlations between adjacent spectrogram cell pairs as moving across the visualizations. This suggests that, in these corresponding regions of \mathbf{E} , the values of neighboring spectrogram values are becoming more similar.

Subsequently, $\hat{\mathbf{E}}$ is analyzed to generate a 3-D mapping $\mathbf{C} \in \mathbb{R}^{N \times N \times 3}$, where the first two dimensions represent each

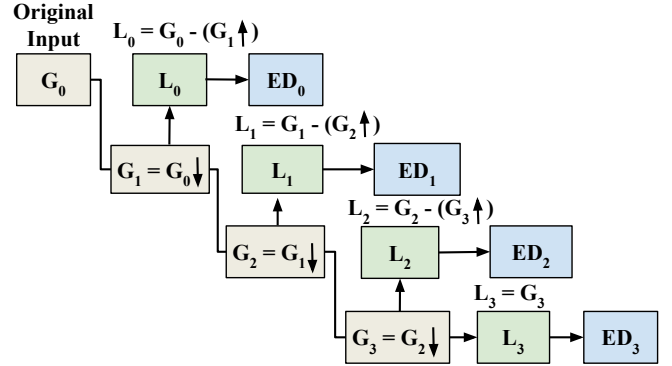


Fig. 3: The steps in the structural module. $\mathbf{L}_0, \mathbf{L}_1, \mathbf{L}_2, \mathbf{L}_3$ represent the high-pass filtered spectrograms generated by the LP decomposition, while $\mathbf{G}_0, \mathbf{G}_1, \mathbf{G}_2, \mathbf{G}_3$ correspond to the low-pass filtered spectrograms produced by the Gaussian Pyramid (GP). $\mathbf{ED}_0, \mathbf{ED}_1, \mathbf{ED}_2, \mathbf{ED}_3$ denote the edge detection filters applied at each level.

possible quantization co-occurrence, and the third dimension signifies the corresponding normalized count. This process is described in Equation 4:

$$\mathbf{C} = \text{Concat} \left(\mathbf{Q}, \frac{\sum_{i=1}^H \sum_{j=1}^W \mathbf{E}_{m,n,i,j}}{\sum_{m=1}^N \sum_{n=1}^N \sum_{i=1}^H \sum_{j=1}^W \mathbf{E}_{m,n,i,j}} \right) \quad (4)$$

Here, $\mathbf{Q} \in \mathbb{R}^{N \times N \times 2}$ represents the pairwise combination of all the quantization levels, where $\mathbf{Q}_{m,n} = [Q_m, Lv_n]$. The process is summarized in Algorithm 1, detailing the steps from cosine similarity calculation to generating the final co-occurrence maps.

Algorithm 1 Statistical Texture Module Processing

INPUT: Feature matrix $\mathbf{A} \in \mathbb{R}^{C \times H \times W}$, RBF parameter γ , quantization levels N
 OUTPUT: 3D co-occurrence map, $\mathbf{C} \in \mathbb{R}^{N \times N \times 3}$

SIMILARITY ESTIMATION

Compute global averaged vector $\mathbf{g} \in \mathbb{R}^{C \times 1 \times 1}$ from \mathbf{A}
 Compute cosine similarity matrix $\mathbf{S} \in \mathbb{R}^{H \times W}$ between \mathbf{g} and each local vector $\mathbf{A}_{[i,j]}$

QUANTIZATION AND EMBEDDING

Quantize \mathbf{S} into N levels: $\mathbf{Q} = \{Q_1, \dots, Q_N\}$
 Compute RBF-based quantized values
 $\mathbf{E} \in \mathbb{R}^{N \times 1 \times H \times W}$

CO-OCCURRENCE CONSTRUCTION

Compute outer product $\hat{\mathbf{E}}_{[i,j]} = \mathbf{E}_{[i,j]} \cdot \mathbf{E}_{[i,j+1]}^T$
 Compute co-occurrence map $\hat{\mathbf{E}} \in \mathbb{R}^{N \times N \times H \times W}$
 Aggregate to form 3D map $\mathbf{C} \in \mathbb{R}^{N \times N \times 3}$

return 3D co-occurrence map, \mathbf{C}

B. Structural Texture Module

Effective texture representation is critical for texture classification, especially when dealing with challenges such as scale variability and complex textural patterns [52]. In the approach used here, structural texture information in the spectral domain is extracted using a novel edge detection module. This module combines hierarchical decomposition techniques, including the LP and edge detection filters, as illustrated in Figure 3.

1) *Laplacian Pyramid Decomposition*: LP is a linear and invertible representation that consists of band-pass images derived from a GP, each representing different scales, along with a low-frequency residual [53]. The downsampling operation, denoted as \downarrow , blurs and reduces the size of a matrix \mathbf{I} , producing a smaller matrix $\mathbf{I} \downarrow$ with half the height and width of the original, as shown in Figure 4. Conversely, the upsampling operation, denoted as \uparrow , smooths and doubles the size of a matrix \mathbf{I} , resulting in a matrix $\mathbf{I} \uparrow$ with dimensions twice that of the input.

To construct the GP $\{\mathbf{G}_0, \mathbf{G}_1, \dots, \mathbf{G}_N\}$, the downsampling operation is applied iteratively to the original image, $\mathbf{G}_0 = \mathbf{I}$ iteratively to generate each subsequent level \mathbf{G}_k . In this case, a 4-level decomposition is used, meaning $N = 4$. The LP $\{\mathbf{L}_0, \mathbf{L}_1, \dots, \mathbf{L}_{N-1}\}$ is created by subtracting the upsampled lower-resolution Gaussian level $\mathbf{G}_{k+1} \uparrow$ from the current level \mathbf{G}_k , as defined in Equation 5:

$$\mathbf{L}_k = \mathbf{G}_k - (\mathbf{G}_{k+1} \uparrow) \quad (5)$$

Each level \mathbf{L}_k captures details at a specific scale, while the final level \mathbf{L}_N represents the low-frequency residual, equivalent to the last level of the GP, \mathbf{G}_N . To reconstruct the original image from the LP, the process is reversed, as shown in Equation 6:

$$\mathbf{G}_k = \mathbf{L}_k + (\mathbf{G}_{k+1} \uparrow) \quad (6)$$

Algorithm 2 Structural Texture Module Processing

INPUT: Feature map $\mathbf{I} \in \mathbb{R}^{C \times H \times W}$, levels N , directional Sobel filters
 OUTPUT: Structural texture representation, $\mathbf{T} \in \mathbb{R}^{C' \times H \times W}$

LAPLACIAN PYRAMID DECOMPOSITION

$\mathbf{G}_0 \leftarrow \mathbf{I}$
for $k = 0$ to $N - 1$ **do**
 $\mathbf{G}_{k+1} \leftarrow \text{Downsample}(\mathbf{G}_k)$
 $\mathbf{L}_k \leftarrow \mathbf{G}_k - \text{Upsample}(\mathbf{G}_{k+1})$
end for
 $\mathbf{L}_N \leftarrow \mathbf{G}_N$ (*low-frequency residual*)

EDGE DETECTION

for each \mathbf{L}_k **do**
 for each direction $\theta \in \{0^\circ, 45^\circ, \dots, 315^\circ\}$ **do**
 $\mathbf{E}_k^\theta \leftarrow \text{Sobel}(\mathbf{L}_k, \theta)$
 end for
end for

EDGE FUSION

(*Option 1*) *Weighted Sum*: $\mathbf{T} \leftarrow \text{GroupedConv}(\{\mathbf{E}_k^\theta\})$
 (*Option 2*) *Max Fusion*: $\mathbf{T} \leftarrow \max_\theta(\mathbf{E}_k^\theta)$
 (*Option 3*) *All Fusion*: $\mathbf{T} \leftarrow \text{Concat}(\mathbf{E}_k^\theta \forall k, \theta)$

return Structural texture representation, \mathbf{T}

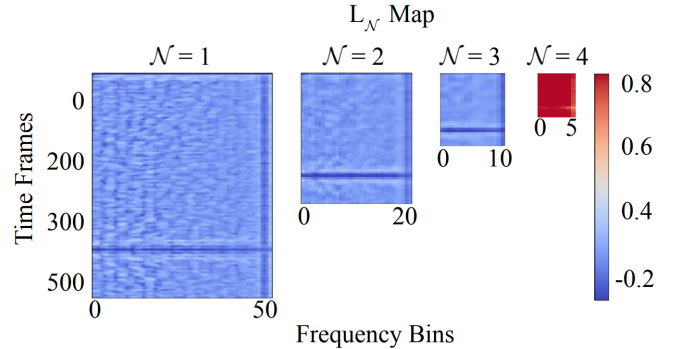


Fig. 4: Visualization of the 4-level LP decomposition stages. This figure illustrates the downsampling process that generates multi-scale Gaussian levels, with the LP capturing the differences between these levels. The decomposition preserves fine details across different scales, highlighting the transitions from finer to coarser resolutions.

The reconstruction process begins with $\mathbf{G}_N = \mathbf{L}_N$ and proceeds by upsampling and adding the difference matrices from finer levels until the full-resolution image \mathbf{G}_0 is restored. This process is visualized in Figure 4.

2) *Edge Detection Filters and Edge Responses*: At each level of the LP, directional information is captured using edge detection filters. Specifically, Sobel kernels [54] are applied to the feature maps at each level to generate edge responses across eight orientations: 0, 45, 90, 135, 180, 225, 270, and 315 degrees. These edge responses emphasize the directional texture patterns, which are crucial for robust texture representation. To aggregate these edge responses into the final

structural texture map \mathbf{T} , three distinct fusion methods are implemented:

- **Weighted Sum:** A grouped convolution combines responses, learning their relative importance.
- **Max:** The strongest edge response is retained by selecting the maximum value across channels.
- **All:** All edge responses are retained, preserving full directional information.

The fused structural texture representation $\mathbf{T} \in \mathbb{R}^{C' \times H \times W}$ captures directional edge patterns across multiple pyramid levels and serves as a rich descriptor for structural texture analysis.

C. Loss Functions in SSTAKD

Distinct loss functions are adopted to balance the objectives of texture analysis and classification.

1) *Statistical Loss:* The three-dimensional feature maps $\mathbf{C} \in \mathbb{R}^{N \times N \times 3}$ generated by the statistical module represent co-occurrence matrices and counts derived from both the teacher and student models. These feature maps capture the distributional characteristics of the models. Since the teacher and student models may have different bin centers and widths for their histograms, direct comparison of their distributions can be challenging. To address this, a 2D histogram-based EMD loss is implemented, which involves computing histograms for both models and using EMD to ensure a fair comparison. First, the 2D histograms for the teacher \mathbf{H}_T and student \mathbf{H}_S models are calculated. These histograms are then normalized to sum to one to form valid probability mass functions.

Next, the cumulative distribution functions (CDFs) for each histogram are calculated by summing the normalized values along both dimensions, as given by Equation 7:

$$\begin{aligned} \text{CDF}_T(x_T, y_T) &= \sum_{i \leq x_T} \sum_{j \leq y_T} \mathbf{H}_T(i, j) \\ \text{CDF}_S(x_S, y_S) &= \sum_{i \leq x_S} \sum_{j \leq y_S} \mathbf{H}_S(i, j) \end{aligned} \quad (7)$$

Here, x_T and y_T represent the coordinates in the teacher model's histogram, while x_S and y_S represent the coordinates in the student model's histogram.

The ground matrix \mathbf{D} is then computed using the Euclidean distances between each pair of 2D bin centers to quantify the differences between the histograms. \mathbf{D} represents the cost of transferring knowledge from the teacher to the student, as defined in Equation 8:

$$\mathbf{D} = \sqrt{(x_T - x_S)^2 + (y_T - y_S)^2} \quad (8)$$

Finally, the statistical loss L_{stat} is defined as the 2D EMD, computed by summing the weighted squared difference between the CDFs of the teacher and student histograms, as shown in Equation 9:

$$L_{\text{stat}} = \sum_{x_T, y_T} \sum_{x_S, y_S} \mathbf{D} \cdot (\text{CDF}_T(x_T, y_T) - \text{CDF}_S(x_S, y_S))^2 \quad (9)$$

2) *Structural Loss:* To quantify the alignment between structural features, the structural loss L_{struct} is defined using cosine similarity. Cosine similarity measures the angle between two vectors, focusing on their directional alignment rather than their magnitude, resulting in an effective metric for comparing structural patterns in the feature space. The objective is to minimize the discrepancy between the structural features of the teacher and student models. Given the feature maps $\mathbf{F} \in \mathbb{R}^{C \times H \times W}$, the cosine similarity is calculated along the feature dimension. Thus, the structural loss L_{struct} is formulated as Equation 10:

$$L_{\text{struct}} = 1 - \text{CosSim}(\mathbf{F}_i^{\text{struct};T}, \mathbf{F}_i^{\text{struct};S}) \quad (10)$$

Here, $\mathbf{F}_i^{\text{struct};T}$ and $\mathbf{F}_i^{\text{struct};S}$ represent the structural feature maps of the teacher and student models for the i -th sample, and the cosine similarity is computed along the channel dimension C .

3) *Classification Loss:* Cross-entropy loss is used to measure the alignment between predicted probabilities and true class labels, as defined in Equation 11:

$$L_{\text{cls}} = - \sum_{i=1}^C y_i \log(p_i) \quad (11)$$

where p represents the predicted probability distribution, y is the one-hot encoded true labels, and C is the number of classes.

4) *Distillation Loss:* To promote response-based knowledge distillation and enable the student to approximate the teacher's soft targets, EMD loss is employed. The bin centers and widths are shared between student and teacher, as they represent softmax logits corresponding to class probability distributions. EMD is well-suited for cases where teacher and student outputs differ in shape or smoothness, particularly when direct layer mappings are infeasible due to architectural differences [55]. EMD quantifies the dissimilarity between probability distributions by calculating the minimum cost required to transform one distribution into another. The distillation loss, L_{distill} , is defined in Equation 12 as the mean squared difference between the CDFs of the student and teacher models:

$$L_{\text{distill}} = \frac{1}{C} \sum_{i=1}^C (\text{CDF}_{\text{student}}(i) - \text{CDF}_{\text{teacher}}(i))^2 \quad (12)$$

where i refers to the class index within the CDFs and C is the number of classes. The sum computes the squared difference between the CDFs of the student and teacher models across C classes for a single sample.

D. Overall Objective Function

Achieving the right balance among objectives is crucial for maximizing the model's overall performance. To achieve this balance, an uncertainty-based loss weighting approach [56] is utilized. This method dynamically adjusts the contribution of each loss component based on the uncertainty of the

corresponding task. The total loss for the SSATKD model is therefore computed using Equation 13:

$$\text{Total Loss} = \alpha_1 \cdot L_{\text{cls}} + \alpha_2 \cdot L_{\text{stat}} + \alpha_3 \cdot L_{\text{struct}} + \alpha_4 \cdot L_{\text{dist}} \quad (13)$$

where α_1 , α_2 , α_3 , and α_4 are the weights assigned to each loss component. These weights are determined based on the variance of each task’s predictions, which reflects the uncertainty in the model’s performance for that task. The weights are computed using Equation 14:

$$\alpha_i = \frac{1}{\sigma_{L_i}^2} + \log(\sigma_{L_i}^2) \quad (14)$$

In this equation, $\sigma_{L_i}^2$ represents the variance associated with the i -th task’s loss component, with higher variance indicating greater uncertainty. By scaling α_i inversely with the precision (the inverse of the variance), the model places more importance on tasks where it has higher confidence and reduces the influence of tasks with greater uncertainty. This uncertainty-based weighting approach eliminates the need for manual tuning of loss weights, allowing the model to automatically balance the different loss components for optimal performance.

IV. EXPERIMENTAL SETUP

A. Data Preparation

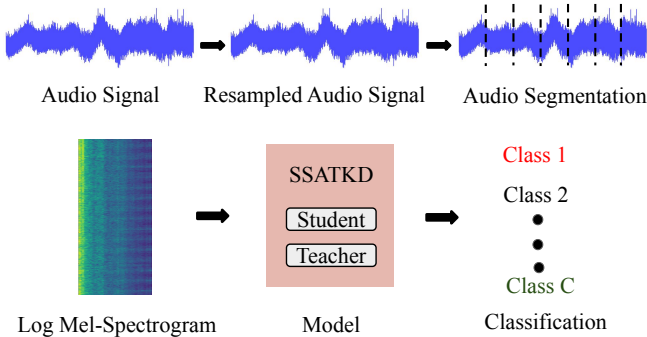


Fig. 5: Data preparation pipeline for the SSATKD framework. The process includes resampling audio signals, segmenting them into fixed-length intervals, and converting them into log Mel-frequency spectrograms used as input to the SSATKD framework.

TABLE I: Summary of datasets used in SSATKD experiments.

Dataset	Total Samples	Classes	Segment Duration
DeepShip	33,770	4	5s
VTUAD	175,965	5	1s
ESC-50	2,000	50	5s
UrbanSound8K	8,732	10	4s

To evaluate the generalizability of the SSATKD framework, to a variety of domains, experiments were conducted on four audio classification datasets: two from the underwater acoustic domain (DeepShip [57] and Vessel Type Underwater Acoustic Data (VTUAD) [58]) and two from environmental audio

(Environmental Sound Classification 50 (ESC-50) [3] and UrbanSound8K [30]). All audio recordings were resampled to 32 kHz to maintain a consistent sampling rate across datasets. To ensure uniform input dimensions for spectrogram extraction, each recording was either segmented, padded, or truncated to a fixed duration, as summarized in Table I.

Recordings in the DeepShip dataset were segmented into 5-second intervals. The ESC-50 and UrbanSound8K datasets were used with their predefined 5-fold and 10-fold splits, respectively, and all UrbanSound8K clips were zero-padded or truncated to a fixed duration of 4 seconds. The VTUAD dataset was used in the combined scenario, utilizing the predefined training, validation, and test partitions provided with the dataset, which consist of 1-second segments. All segments were transformed into log Mel-frequency spectrograms using a Hann window of size 1024, a hop length of 320, and 64 mel filters. SpecAugmentation [59] was applied during training by randomly masking time and frequency bands to improve robustness. These spectrograms served as input to the SSATKD framework. The overall data preparation pipeline is illustrated in Figure 5.

B. Implementation Details

The HLTDNN model is fixed as the student model in all experiments. For the teacher model, six architectures were evaluated. Three convolutional models from the Pre-trained Audio Neural Network (PANNs) family [60]: CNN14, ResNet38, and MobileNetV1 were selected due to their strong performance in the original PANN benchmark. In addition, three large-scale audio foundation models were included: Wav2Vec 2.0 (Base) [61], HuBERT (Base) [62], and Whisper (Small) [63]. These models represent transformer-based or hybrid (CNN + transformer) encoder architectures trained on diverse speech or audio tasks, offering an opportunity to study generalization in cross-domain distillation.

To investigate the effect of teacher adaptation, two training regimes were considered: (1) training only the output classification layer of the teacher model while freezing all preceding layers, and (2) full fine-tuning of the teacher model on each target dataset before knowledge distillation. All models are trained across four datasets: DeepShip, VTUAD, ESC-50, and UrbanSound8K. The AdamW optimizer is used with an initial learning rate of 0.0001, which is adjusted using a learning rate schedule defined in Equation 15

$$\text{lr} \times \left(1 - \frac{\text{iter}}{\text{max_iter}}\right)^{0.9} \quad (15)$$

Training is performed for up to 150 epochs with early stopping based on validation performance, using a patience of 50 epochs and batch size of 32. All experiments are repeated across three independent runs using different random seeds, and average results with standard deviations are reported.

V. RESULTS AND DISCUSSION

A. Baseline Classification Performance

Table II summarizes the baseline classification accuracy of the student model, a histogram layer time-delay neural

TABLE II: Baseline classification accuracy (%) and model size for the student model (HLTDNN) and teacher models across four datasets. Values represent the average and standard deviation over three independent runs. The best accuracy for each dataset is highlighted in bold.

Model Type	Model Name	# Parameters	Classification Accuracy (%)			
			DeepShip	VTUAD	ESC-50	UrbanSound8K
Student Model	HLTDNN	11.3K	59.62 ± 1.69	80.49 ± 1.77	72.33 ± 0.76	88.14 ± 0.20
Teacher Model	CNN14	79.7M	71.33 ± 1.21	96.91 ± 0.32	84.01 ± 1.21	96.45 ± 1.21
	ResNet38	72.7M	64.93 ± 1.52	97.88 ± 0.26	80.23 ± 1.33	93.50 ± 1.43
	MobileNetV1	4.3M	66.64 ± 1.92	95.53 ± 0.33	82.07 ± 1.51	98.87 ± 1.98
	Wav2Vec 2.0	95.0M	63.26 ± 0.01	94.22 ± 0.84	82.31 ± 1.49	95.68 ± 1.06
	HuBERT	95.7M	63.73 ± 0.01	95.18 ± 0.71	83.56 ± 1.09	96.24 ± 1.98
	Whisper	74.0M	66.91 ± 0.03	93.35 ± 0.62	88.84 ± 1.28	94.33 ± 1.88

TABLE III: SSATKD classification accuracy (%) with classifier-head-only teacher adaptation. Each teacher model was partially adapted by training only the output layer while freezing the rest of the network. Results are averaged over three independent runs. A 1×1 convolution was added to align teacher and student feature maps, increasing HLTDNN parameters from 11.3K to 12.3K. The last column shows the average gain in accuracy over the baseline HLTDNN across the four datasets.

Model	# Parameters (Student vs. Teacher)	Classification Accuracy (%)				Avg. Gain (%)
		DeepShip	VTUAD	ESC-50	UrbanSound8K	
Student Only	11.3K	59.62 ± 1.69	80.49 ± 1.77	72.33 ± 0.76	88.14 ± 0.20	N/A
Student + CNN14	12.3K vs. 79.7M	63.16 ± 1.22	80.97 ± 0.47	77.55 ± 1.71	89.52 ± 0.33	+2.91
Student + ResNet38	12.3K vs. 72.7M	62.43 ± 1.81	83.03 ± 0.69	72.45 ± 1.53	88.67 ± 0.29	+1.75
Student + MobileNetV1	12.3K vs. 4.3M	63.55 ± 1.50	80.68 ± 1.04	73.58 ± 1.19	89.74 ± 0.27	+1.99
Student + Wav2Vec 2.0	12.3K vs. 95.0M	60.95 ± 1.06	81.93 ± 0.63	74.81 ± 1.42	88.92 ± 0.24	+1.51
Student + HuBERT	12.3K vs. 95.7M	62.11 ± 1.32	82.41 ± 0.52	75.73 ± 1.38	89.21 ± 0.28	+2.22
Student + Whisper	12.3K vs. 74.0M	63.51 ± 1.46	81.77 ± 0.74	76.83 ± 1.55	90.03 ± 0.30	+2.92

network (HLTDNN), and six teacher models across four datasets. The HLTDNN model, with only 11.3K parameters, consistently achieves reasonable accuracy despite its compact architecture. Its performance is statistically significantly lower than the teacher models, but its low computational costs (e.g., number of learnable parameters) make it suitable for resource-constrained environments. Among the teacher models, CNN14 achieves the highest accuracy on the DeepShip dataset with 71.33%, leveraging its large capacity of 79.7M parameters. ResNet38, although similarly large with 72.7M parameters, outperforms all models on VTUAD with 97.88%, highlighting its effectiveness in classifying short underwater acoustic segments. MobileNetV1, the most lightweight among the teacher models at 4.3M parameters, attains the highest accuracy on UrbanSound8K at 98.87%. This suggests that MobileNetV1 balances efficiency and performance well for environmental sound tasks. All three models were pretrained on a large-scale, widely used audio dataset, AudioSet [64], with full supervision, which contributes to robustness across the different environmental sound datasets, particularly the passive sonar datasets, as other work has shown [65].

Whisper (Small), with 74M parameters, achieves the highest accuracy on the ESC-50 dataset with 88.84%, outperforming all other teacher models. While Wav2Vec 2.0 (Base) and HuBERT (Base) show competitive performance across all datasets, they do not achieve the top result for any dataset. These models were pretrained using self-supervised learning (SSL), which enables general representation learning and robustness. However, unlike the PANN models that were trained with full supervision on AudioSet, these SSL models

are not specifically optimized for audio event classification tasks. This may explain why the PANN models outperform Whisper and the SSL models in passive sonar classification, despite having a similar or even smaller number of parameters. This observation indicates that while large-scale pretraining contributes to general robustness, domain-specific optimization and supervised learning play an important role in maximizing performance on a given task. Overall, the baseline results confirm expected trends. Larger models such as CNN14 and ResNet38 deliver strong performance in passive sonar classification, while Whisper and MobileNetV1 provide competitive results in general environmental audio. The HLTDNN student model offers an efficient alternative at a significantly reduced scale, which is further enhanced in subsequent SSATKD experiments.

B. SSATKD Classification Performance

1) *Classifier-Head-Only Teacher Adaptation*: Table III reports the classification accuracy of the SSATKD framework when each teacher model is partially adapted by training only the final output layer while keeping all other layers frozen. The student model remains HLTDNN across all configurations. Despite the limited adaptation of the teacher, SSATKD consistently improves performance over the baseline student model across all datasets. On the DeepShip dataset, MobileNetV1 achieves the highest accuracy (63.55%), slightly outperforming CNN14 and Whisper. For VTUAD, ResNet38 achieves the top accuracy (83.03%), likely benefiting from its deep convolutional architecture, which is well suited to short and repetitive underwater signal segments. On the ESC-50

TABLE IV: SSATKD classification accuracy (%) with full teacher fine-tuning. Each teacher model was fully adapted to the target dataset prior to distillation. Results are averaged over three independent runs. The last column shows the average gain in accuracy over the baseline HLTDNN across the four datasets.

Model	# Parameters (Student vs. Teacher)	Classification Accuracy (%)				Avg. Gain (%)
		DeepShip	VTUAD	ESC-50	UrbanSound8K	
Student Only	11.3K	59.62 ± 1.69	80.49 ± 1.77	72.33 ± 0.76	88.14 ± 0.20	N/A
Student + CNN14	12.3K vs. 79.7M	64.72 ± 1.92	85.35 ± 0.75	80.33 ± 1.25	91.84 ± 0.55	+5.42
Student + ResNet38	12.3K vs. 72.7M	65.62 ± 1.75	86.11 ± 0.73	78.81 ± 1.18	90.71 ± 0.55	+4.72
Student + MobileNetV1	12.3K vs. 4.3M	66.22 ± 0.83	84.40 ± 0.85	79.50 ± 1.66	91.62 ± 0.53	+5.29
Student + Wav2Vec 2.0	12.3K vs. 95.0M	64.20 ± 1.61	85.17 ± 0.65	79.26 ± 1.05	90.11 ± 0.45	+4.34
Student + HuBERT	12.3K vs. 95.7M	65.11 ± 1.55	86.50 ± 0.62	80.04 ± 1.10	90.95 ± 0.51	+5.23
Student + Whisper	12.3K vs. 74.0M	66.12 ± 1.80	85.23 ± 0.71	80.21 ± 1.27	91.84 ± 0.61	+5.33

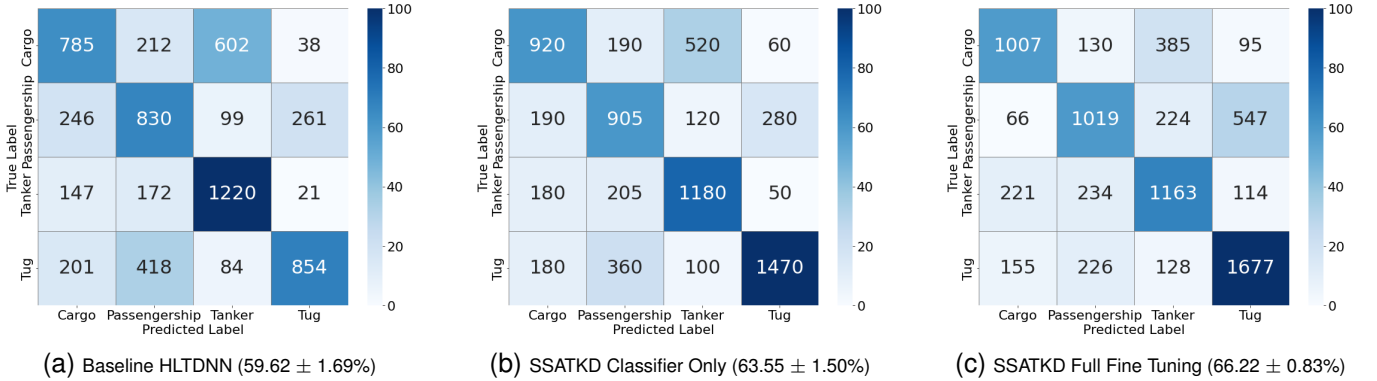


Fig. 6: Performance comparison of HLTDNN baseline and SSATKD under two adaptation settings on DeepShip. (a) Baseline HLTDNN. (b) Classifier-only adaptation. (c) Full fine-tuning.

dataset, CNN14 leads with 77.55%, indicating that PANN-based CNN architectures still retain strong feature extraction capabilities for general environmental sound classification, even under partial adaptation.

For UrbanSound8K, Whisper (Small) achieves the highest accuracy (90.03%), suggesting that transformer-based models with diverse pretraining still provide strong generalization under minimal tuning. Wav2Vec 2.0 and HuBERT also deliver competitive performance across datasets, showing that SSATKD can effectively leverage representations from both convolutional and transformer-based teachers. Overall, these results indicate that the SSATKD framework is capable of enhancing a lightweight student model even when the teacher is only partially adapted to the target domain. This makes it a practical and efficient choice for scenarios with limited computational resources or adaptation constraints.

2) *Full Teacher Fine-Tuning*: Table IV presents the classification results when each teacher model is fully fine-tuned on the target dataset before applying SSATKD. Compared to the classifier-head-only setup, this configuration consistently improves student model accuracy across all datasets. MobileNetV1 achieves the best performance (66.22%), closely followed by Whisper (66.12%) and ResNet38 (65.62%). For VTUAD, the highest accuracy is obtained by HuBERT (Base) (86.50%), suggesting that transformer-based models can be particularly effective in sonar classification when fully adapted to the task.

In environmental audio tasks, CNN14 achieves the best per-

formance on ESC-50 (80.33%), narrowly surpassing Whisper and HuBERT. For UrbanSound8K, both CNN14 and Whisper achieve the top score (91.84%), suggesting their complementary strengths in modeling diverse soundscapes. Overall, full fine-tuning of the teacher results in consistent accuracy improvements across all domains. While CNN14 remains highly competitive, foundation models like Whisper and HuBERT demonstrate strong generalization when given sufficient task-specific adaptation. These findings validate the effectiveness of SSATKD under more flexible teacher configurations and highlight its capacity to improve performance even in compact student models.

The evaluation under both classifier-only and full fine-tuning settings highlights the flexibility of the SSATKD framework across different training budgets. While full fine-tuning consistently leads to the highest student accuracy, the classifier-only approach still yields substantial gains with minimal teacher adaptation. For example, using MobileNetV1 on the DeepShip dataset, SSATKD improves over the HLTDNN baseline by +3.93% with classifier-only training and by +6.60% under full fine-tuning. Similar patterns are observed across other datasets, demonstrating that even partial adaptation of the teacher is sufficient to extract meaningful structure and statistical cues for student transfer. This makes SSATKD practical for scenarios with limited resources, while still scalable to high-performance settings.

For class-wise performance visualization, the DeepShip dataset and the MobileNetV1–HLTDNN teacher-student pair

were selected. DeepShip presents a representative passive sonar classification scenario characterized by moderate inter-class overlap and realistic underwater acoustic conditions, making it suitable for confusion matrix analysis. MobileNetV1 was chosen as the teacher model due to its strong trade-off between model size and performance, consistently demonstrating competitive accuracy across all datasets. Figure 6 shows the confusion matrices for three settings: (a) baseline HLTDDN, (b) SSATKD with classifier-only adaptation, and (c) SSATKD with full teacher fine-tuning. Both adaptation strategies improve class-wise discrimination, particularly for classes such as Tug and Passengership, with full fine-tuning providing the clearest separation.

C. Ablation study

To analyze the contributions of individual SSATKD components, ablation experiments were conducted using the DeepShip dataset with MobileNetV1 as the teacher model. This configuration was selected as a representative case due to its competitive performance, efficient architecture, and the fact that DeepShip was the most challenging dataset for all models. It offers a balanced setup for studying the impact of statistical and structural texture distillation on student model performance.

1) *Distillation Loss Comparison*: To evaluate the impact of the distillation loss function, we compare the performance of the widely used Kullback-Leibler divergence (KLDiv) loss and EMD loss. Both losses are used to align the output distributions between the teacher and student models, but they differ in how they measure distributional discrepancies.

TABLE V: Comparison of KLDiv and EMD as distillation loss functions. Results show the improvement in using EMD over KLDiv in model accuracy.

Distillation Loss	Accuracy
KLDiv	64.02 \pm 0.14%
EMD	65.99 \pm 0.59%

As shown in Table V, the EMD-based distillation achieved a statistically significant difference from KLDiv. This indicates that EMD, by accounting for the underlying geometry of the sample space when comparing distributions, offers a more informative supervisory signal for aligning teacher and student outputs.

2) *Temperature Parameter Tuning*: The temperature parameter in knowledge distillation controls the softness of the softmax outputs from the teacher model. Higher temperatures produce smoother probability distributions, making it easier for the student model to learn fine-grained knowledge. The temperature can either be fixed or set as a learnable parameter. Common fixed values include 1 and 2, while learnable approaches involve initializing temperature values and updating them during training.

The results in Table VI show that both fixed and learnable temperature strategies yield competitive performance. Among learnable methods, initializing with 1 provides the most stable and accurate results. In contrast, initializing with 2 and sharpness-based adaptation leads to higher variance, suggesting instability in those configurations.

TABLE VI: Comparison of different distillation temperature tuning methods on model accuracy. Results show the impact of fixed and learnable temperature approaches. The highest accuracy, highlighted in bold, was achieved using the 'Learnable - Initialized with 1' method.

Tuning Method	Accuracy
Fixed to 1	64.99 \pm 0.77%
Fixed to 2	65.87 \pm 1.91%
Learnable - Initialized with 1	65.87 \pm 1.26%
Learnable - Initialized with 2	60.27 \pm 9.58%
Learnable - Sharpness Based	61.36 \pm 4.19%

TABLE VII: Effect of statistical, structural, and distillation loss combinations on model accuracy. The table illustrates how different combinations of loss components influence model performance, highlighting the contribution of each component. The highest accuracy, highlighted in bold, was achieved by combining structural and distillation loss without the statistical loss.

Statistical	Structural	Distillation	Accuracy
			59.62 \pm 1.69%
		✓	65.99 \pm 0.59%
	✓		65.80 \pm 0.52%
	✓	✓	67.46 \pm 0.91%
✓			65.43 \pm 0.60%
✓		✓	61.85 \pm 0.52%
✓	✓		64.84 \pm 1.45%
✓	✓	✓	66.22 \pm 0.83%

3) *Analysis of loss components*: Table VII presents the impact of various combinations of structural, statistical, and distillation loss terms on the accuracy of the HLTDDN student model, with classification loss applied in all cases. The baseline accuracy with only classification loss is 59.62%. Incorporating the distillation loss alone boosts performance to 65.99%, highlighting the advantage of knowledge transfer from the teacher model. Similarly, the addition of statistical loss alone increases accuracy to 65.80%, indicating that statistical alignment also contributes positively to performance. However, combining both statistical and distillation losses results in a decrease to 61.85%, suggesting possible interference between these two losses when applied together.

When the structural loss is combined with classification loss, the accuracy improves to 65.43%. The combination of structural and distillation losses achieves the highest accuracy of 67.46%, showing the strong interaction between these losses. The pairing of structural and statistical losses results in a slightly lower accuracy of 64.84%. Lastly, applying all three losses together produces an accuracy of 66.22%. The results show that each loss term helps improve accuracy on its own. However, when combined, certain combinations work better than others. The structural and distillation losses together led to the biggest improvement, whereas the statistical and distillation losses together reduced accuracy. This drop in performance may be due to the equal bin size configuration to learn the statistical textures of the data. By using leveraging learnable bin centers and widths via backpropagation [54], future experiments could potentially improve performance with minimal overhead.

4) *Analysis of Structural Module*: Table VIII presents the performance of different fusion modes in the structural mod-

ule. The ‘‘All Fusion’’ method achieved the highest accuracy of 66.22%, demonstrating the effectiveness of retaining all edge responses from different orientations to capture comprehensive texture information. The ‘‘Max Fusion’’ method, which selects the strongest edges, reached 65.38%, but may have missed some finer details. The ‘‘Weighted Sum Fusion’’ method resulted in 61.77%, likely due to potential loss of directional information during linear combination. Overall, the ‘‘All Fusion’’ method provided the best balance between accuracy and model complexity.

TABLE VIII: Impact of different fusion modes on test accuracy and model parameters. The highest accuracy, highlighted in bold, was achieved using the ‘‘All Fusion’’ mode.

Fusion Mode	Accuracy	Params
All	66.22 ± 0.83%	12.3 K
Max	65.38 ± 0.58%	12.3 K
Weighted Sum	61.77 ± 1.21%	14.6 K

Table IX shows the impact of decomposition levels. A 4-level decomposition produced the best results with 66.22%, while using fewer (2 levels) led to slightly lower accuracy (64.82%). Increasing to 8 levels reduced accuracy to 61.77%, likely due to overfitting or unnecessary complexity. This suggests that while multi-level decomposition captures valuable structural details, there is an optimal balance between complexity and performance, with 4 levels proving to be the most effective in the case of these experiments.

TABLE IX: Effect of decomposition levels on model accuracy. The highest accuracy, highlighted in bold, was achieved at 4 decomposition levels.

Decomposition Levels	Accuracy
2	64.82 ± 0.28%
4	66.22 ± 0.83%
8	61.77 ± 1.21%

5) *Analysis of Statistical Module*: Table X compares the performance of linear and RBF quantization methods. RBF quantization outperformed linear, achieving 65.87% accuracy compared to 61.77%. This suggests that RBF provides a smoother and more precise representation, whereas the simpler linear method is less effective at handling finer details in the data.

TABLE X: Effect of binning methods on model accuracy. The highest accuracy, highlighted in bold, was achieved using the RBF binning method.

Bining Method	Accuracy
Linear	61.77 ± 1.42%
RBF	65.87 ± 1.26%

Table XI shows the impact of the number of quantization levels. Accuracy peaks at 66.22% with 4 levels, indicating that a moderate level of quantization effectively captures essential details. Increasing the levels to 16 and 32 leads to a performance drop, likely due to overfitting or sensitivity to minor variations. Thus, while finer quantization helps, too many levels can degrade performance.

TABLE XI: Effect of quantization levels and bins on model accuracy. The highest accuracy, highlighted in bold, was achieved using 4 quantization levels.

Number of Levels/Bins	Accuracy
2	61.83 ± 6.71%
4	66.22 ± 0.83%
8	65.87 ± 1.26%
16	61.84 ± 2.15%
32	43.45 ± 5.13%

TABLE XII: Performance comparison of SSATKD with various knowledge distillation methods using the `torchdistill` framework [71] on the Deepship dataset. Metrics include accuracy, precision, recall, and F1-score, averaged over three runs, with best performances in bold.

Method	Accuracy	Precision	Recall	F1-score
SRD [66]	61.99 ± 1.52%	62.50 ± 1.64%	62.32 ± 1.66%	61.93 ± 1.82%
TF-KD [67]	60.33 ± 1.72%	60.51 ± 1.10%	59.54 ± 1.31%	60.23 ± 1.02%
CRD [68]	61.42 ± 1.87%	63.33 ± 1.41%	60.82 ± 1.92%	62.12 ± 1.77%
PAD [69]	52.25 ± 1.33%	53.54 ± 1.27%	52.77 ± 1.26%	52.53 ± 1.22%
CCKD [70]	60.13 ± 1.68%	60.54 ± 1.81%	58.45 ± 1.12%	60.73 ± 1.42%
SSATKD (Ours)	65.92 ± 1.18%	67.65 ± 1.21%	66.32 ± 0.88%	67.18 ± 1.22%

D. Comparison with Existing State-of-the-Art Knowledge Distillation Methods

The proposed SSATKD was compared against five state-of-the-art knowledge distillation methods: Semantic Representational Distillation (SRD) [66], Teacher-Free Knowledge Distillation (TF-KD) [67], Contrastive Representation Distillation (CRD) [68], Prime-Aware Adaptive Distillation (PAD) [69], and Correlation Congruence for Knowledge Distillation (CCKD) [70]. These methods were selected based on their recent implementation in the `torchdistill` framework [71], which provides a robust and up-to-date benchmark for a fair evaluation. Each method uses the same teacher-student configuration: MobileNetV1 as the teacher and HLTDDN as the student. SSATKD was also re-evaluated within the `torchdistill` framework to maintain identical training conditions. The results of this comparison are summarized in Table XII. As shown, SSATKD demonstrates better performance across all metrics, demonstrating the proposed method’s effectiveness relative to existing methods.

SSATKD’s advantages over other methods stem from its unique combination of texture modeling and diversity preservation, both of which enhance the student model’s ability to learn detailed and comprehensive representations. Compared to SRD, which aligns individual semantic features between teacher and student, SSATKD captures relationships across multiple scales via structural texture features. SRD’s alignment approach cannot model complex, high-dimensional dependencies, limiting the richness of learned representations [72]. SSATKD’s Edge Detection Module (EDM) preserves spatial context across feature levels, allowing the student to learn more effectively.

TF-KD, while effective without a teacher, lacks the benefit of structured knowledge transfer from a pre-trained model. Without a teacher, TF-KD cannot explicitly transfer the structural and statistical knowledge embedded in trained networks. In contrast, SSATKD leverages the teacher to transfer both low-level structural features (via edge detection) and statistical measures (via texture quantization), enabling more compre-

hensive knowledge transfer.

CRD captures relational information by maximizing mutual information between teacher and student, but it often requires large batch sizes and extensive training [73]. Moreover, CRD focuses only on structural relations. SSATKD, on the other hand, captures both structural texture and statistical diversity using RBF-based quantization, allowing the student to learn richer feature representations. PAD prioritizes low-uncertainty “prime” samples, but this selective weighting can reduce generalizability by overlooking rare or complex patterns [74]. SSATKD avoids this bias by modeling texture features across all samples, leading to more robust generalization.

Finally, CCKD aligns relational information and captures some inter-channel correlation but lacks a holistic mechanism to preserve feature diversity [75]. SSATKD addresses this by modeling inter-channel correlations across multiple orientations and scales and by preserving diversity through the statistical texture module. Together, these components enable SSATKD to capture a more complete range of relational and structural features, leading to consistent performance gains.

VI. CONCLUSION

This work introduced SSATKD, a texture-aware knowledge distillation framework that transfers both low-level audio textures and high-level semantic responses from teacher to student models. The results highlight that combining structural and distillation losses yields the highest gains, with response-based distillation playing a dominant role in performance. Comparisons with recent knowledge distillation methods further validated the effectiveness of SSATKD’s hybrid texture-response transfer strategy. This framework has potential to be beneficial for real-time environmental monitoring systems or edge devices where large models are impractical. Future work could explore adaptive loss balancing, expand to other domains like bioacoustics, and integrate self-supervised or multimodal learning to improve generalization and deployment efficiency.

REFERENCES

- [1] K. Xu, Q. Xu, K. You, B. Zhu, M. Feng, D. Feng, and B. Liu, “Self-supervised learning-based underwater acoustical signal classification via mask modeling,” *The Journal of the Acoustical Society of America*, vol. 154, no. 1, pp. 5–15, 2023.
- [2] S. Wang and X. Zeng, “Robust underwater noise targets classification using auditory inspired time-frequency analysis,” *Applied Acoustics*, vol. 78, pp. 68–76, 2014.
- [3] K. J. Piczak, “Esc: Dataset for environmental sound classification,” in *Proceedings of the 23rd ACM international conference on Multimedia*, 2015, pp. 1015–1018.
- [4] J. Ghosh, K. Turner, S. Beck, and L. Deuser, “Integration of neural classifiers for passive sonar signals,” in *Control and Dynamic Systems*. Elsevier, 1996, vol. 77, pp. 301–338.
- [5] D. Neupane and J. Seok, “A review on deep learning-based approaches for automatic sonar target recognition,” *Electronics*, vol. 9, no. 11, p. 1972, 2020.
- [6] G. Li, W. Bu, and H. Yang, “Noise reduction method for ship radiated noise signal based on modified uniform phase empirical mode decomposition,” *Measurement*, vol. 227, p. 114193, 2024.
- [7] Z. Lian, K. Xu, J. Wan, and G. Li, “Underwater acoustic target classification based on modified gfcc features,” in *2017 IEEE 2nd Advanced Information Technology, Electronic and Automation Control Conference (IAEAC)*. IEEE, 2017, pp. 258–262.
- [8] X. Luo, L. Chen, H. Zhou, and H. Cao, “A survey of underwater acoustic target recognition methods based on machine learning,” *Journal of Marine Science and Engineering*, vol. 11, no. 2, p. 384, 2023.
- [9] M. A. R. Hashmi and R. H. Raza, “Novel DEMON spectra analysis techniques and empirical knowledge based reference criterion for acoustic signal classification,” *Journal of Electrical Engineering & Technology*, vol. 18, no. 1, pp. 561–578, 2023.
- [10] G. Hinton, O. Vinyals, and J. Dean, “Distilling the knowledge in a neural network,” in *NIPS Deep Learning and Representation Learning Workshop*, 2015. [Online]. Available: <http://arxiv.org/abs/1503.02531>
- [11] Z. Allen-Zhu and Y. Li, “Towards understanding ensemble, knowledge distillation and self-distillation in deep learning,” *arXiv preprint arXiv:2012.09816*, 2020.
- [12] A. Gordon, E. Eban, O. Nachum, B. Chen, H. Wu, T.-J. Yang, and E. Choi, “Morphnet: Fast & simple resource-constrained structure learning of deep networks,” in *Proceedings of the IEEE conference on computer vision and pattern recognition*, 2018, pp. 1586–1595.
- [13] J. Wu, C. Leng, Y. Wang, Q. Hu, and J. Cheng, “Quantized convolutional neural networks for mobile devices,” in *Proceedings of the IEEE conference on computer vision and pattern recognition*, 2016, pp. 4820–4828.
- [14] Y. Cheng, D. Wang, P. Zhou, and T. Zhang, “A survey of model compression and acceleration for deep neural networks,” *arXiv preprint arXiv:1710.09282*, 2017.
- [15] C. Bucilua, R. Caruana, and A. Niculescu-Mizil, “Model compression,” in *Proceedings of the 12th ACM SIGKDD international conference on Knowledge discovery and data mining*, 2006, pp. 535–541.
- [16] L. Beyer, X. Zhai, A. Royer, L. Markeeva, R. Anil, and A. Kolesnikov, “Knowledge distillation: A good teacher is patient and consistent,” in *Proceedings of the IEEE/CVF conference on computer vision and pattern recognition*, 2022, pp. 10925–10934.
- [17] T. Huang, Y. Zhang, M. Zheng, S. You, F. Wang, C. Qian, and C. Xu, “Knowledge diffusion for distillation,” *Advances in Neural Information Processing Systems*, vol. 36, 2024.
- [18] C. Shu, Y. Liu, J. Gao, Z. Yan, and C. Shen, “Channel-wise knowledge distillation for dense prediction,” in *Proceedings of the IEEE/CVF International Conference on Computer Vision*, 2021, pp. 5311–5320.
- [19] S. Yang, A. Jin, X. Zeng, H. Wang, X. Hong, and M. Lei, “Underwater acoustic target recognition based on knowledge distillation under working conditions mismatching,” *Multimedia Systems*, vol. 30, no. 1, p. 12, 2024.
- [20] J. Salamon and J. P. Bello, “Deep convolutional neural networks and data augmentation for environmental sound classification,” *IEEE Signal Processing Letters*, vol. 24, no. 3, pp. 279–283, 2017.
- [21] B. Julesz, “Visual pattern discrimination,” *IRE transactions on Information Theory*, vol. 8, no. 2, pp. 84–92, 1962.
- [22] G. Srinivasan and G. Shobha, “Statistical texture analysis,” in *Proceedings of world academy of science, engineering and technology*, vol. 36, no. December, 2008, pp. 1264–1269.
- [23] J. S. Lim, *Two-dimensional signal and image processing*. Prentice-Hall, Inc., 1990.
- [24] M. Trevorrow, “Examination of statistics and modulation of underwater acoustic ship signatures,” 2021.
- [25] G. Yu and J.-J. Slotine, “Fastwavelet-based visual classification,” in *2008 19th International Conference on Pattern Recognition*. IEEE, 2008, pp. 1–5.
- [26] T. Serre, L. Wolf, S. Bileschi, M. Riesenhuber, and T. Poggio, “Robust object recognition with cortex-like mechanisms,” *IEEE transactions on pattern analysis and machine intelligence*, vol. 29, no. 3, pp. 411–426, 2007.
- [27] X. Yin, X. Sun, P. Liu, L. Wang, and R. Tang, “Underwater acoustic target classification based on lofar spectrum and convolutional neural network,” in *Proceedings of the 2nd International Conference on Artificial Intelligence and Advanced Manufacture*, 2020, pp. 59–63.
- [28] L. C. Domingos, P. E. Santos, P. S. Skelton, R. S. Brinkworth, and K. Sammut, “A survey of underwater acoustic data classification methods using deep learning for shoreline surveillance,” *Sensors*, vol. 22, no. 6, p. 2181, 2022.
- [29] J. McDermott and E. Simoncelli, “Sound texture perception via statistics of the auditory periphery,” 2011.
- [30] J. Salamon, C. Jacoby, and J. P. Bello, “A dataset and taxonomy for urban sound research,” in *Proceedings of the 22nd ACM international conference on Multimedia*, 2014, pp. 1041–1044.
- [31] Y. Tokozume, Y. Ushiku, and T. Harada, “Learning from between-class examples for deep sound recognition,” *arXiv preprint arXiv:1711.10282*, 2017.
- [32] Y. Gong, Y.-A. Chung, and J. Glass, “Ast: Audio spectrogram transformer,” *arXiv preprint arXiv:2104.01778*, 2021.

- [33] K. I. Tan, S. Yean, and B. S. Lee, "Attention-based sound classification pipeline with sound spectrum," in *2023 IEEE Sensors Applications Symposium (SAS)*. IEEE, 2023, pp. 1–6.
- [34] V.-S. Doan, T. Huynh-The, and D.-S. Kim, "Underwater acoustic target classification based on dense convolutional neural network," *IEEE Geoscience and Remote Sensing Letters*, vol. 19, pp. 1–5, 2020.
- [35] R. Akter, M. R. Islam, S. K. Debnath, P. K. Sarker, and M. K. Uddin, "A hybrid cnn-lstm model for environmental sound classification: Leveraging feature engineering and transfer learning," *Digital Signal Processing*, vol. 163, p. 105234, 2025.
- [36] L. Chen, X. Luo, and H. Zhou, "A ship-radiated noise classification method based on domain knowledge embedding and attention mechanism," *Engineering Applications of Artificial Intelligence*, vol. 127, p. 107320, 2024.
- [37] H. I. Hummel, R. van der Mei, and S. Bhulai, "A survey on machine learning in ship radiated noise," *Ocean Engineering*, vol. 298, p. 117252, 2024.
- [38] C. Tan, F. Sun, T. Kong, W. Zhang, C. Yang, and C. Liu, "A survey on deep transfer learning," in *Artificial Neural Networks and Machine Learning—ICANN 2018: 27th International Conference on Artificial Neural Networks, Rhodes, Greece, October 4-7, 2018, Proceedings, Part III 27*. Springer, 2018, pp. 270–279.
- [39] K. Weiss, T. M. Khoshgoftaar, and D. Wang, "A survey of transfer learning," *Journal of Big data*, vol. 3, pp. 1–40, 2016.
- [40] A. Diment and T. Virtanen, "Transfer learning of weakly labelled audio," in *2017 IEEE Workshop on Applications of Signal Processing to Audio and Acoustics (waspa)*. IEEE, 2017, pp. 6–10.
- [41] J. Yim, D. Joo, J. Bae, and J. Kim, "A gift from knowledge distillation: Fast optimization, network minimization and transfer learning," in *Proceedings of the IEEE conference on computer vision and pattern recognition*, 2017, pp. 4133–4141.
- [42] A. M. Tripathi and K. Paul, "Data augmentation guided knowledge distillation for environmental sound classification," *Neurocomputing*, vol. 489, pp. 59–77, 2022.
- [43] J. Pons and X. Serra, "Training neural audio classifiers with few data," *ICASSP 2019 - IEEE International Conference on Acoustics, Speech and Signal Processing (ICASSP)*, pp. 16–20, 2019.
- [44] Y. Gong, Q. Kong, and W. Wang, "Psla: Improving audio tagging with pretrained scalable label assignment," in *ICASSP 2021 - IEEE International Conference on Acoustics, Speech and Signal Processing (ICASSP)*. IEEE, 2021, pp. 321–325.
- [45] F. Liu, H. Ding, D. Li, T. Wang, Z. Luo, and L. Chen, "Few-shot learning with data enhancement and transfer learning for underwater target recognition," in *2021 OES China Ocean Acoustics (COA)*. IEEE, 2021, pp. 992–994.
- [46] D. Cook, K. D. Feuz, and N. C. Krishnan, "Transfer learning for activity recognition: A survey," *Knowledge and information systems*, vol. 36, pp. 537–556, 2013.
- [47] K. Choi, M. Kersner, J. Morton, and B. Chang, "Temporal knowledge distillation for on-device audio classification," in *ICASSP 2022-2022 IEEE International Conference on Acoustics, Speech and Signal Processing (ICASSP)*. IEEE, 2022, pp. 486–490.
- [48] J.-W. Jung, H.-S. Heo, H.-J. Shim, and H.-J. Yu, "Knowledge distillation in acoustic scene classification," *IEEE Access*, vol. 8, pp. 166 870–166 879, 2020.
- [49] D. Ji, H. Wang, M. Tao, J. Huang, X.-S. Hua, and H. Lu, "Structural and statistical texture knowledge distillation for semantic segmentation," in *Proceedings of the IEEE/CVF Conference on Computer Vision and Pattern Recognition*, 2022, pp. 16 876–16 885.
- [50] L. Zhu, D. Ji, S. Zhu, W. Gan, W. Wu, and J. Yan, "Learning statistical texture for semantic segmentation," in *Proceedings of the IEEE/CVF Conference on Computer Vision and Pattern Recognition*, 2021, pp. 12 537–12 546.
- [51] J. Ritu, E. Barnes, R. Martell, A. Van Dine, and J. Peeples, "Histogram layer time delay neural networks for passive sonar classification," in *2023 IEEE Workshop on Applications of Signal Processing to Audio and Acoustics (WASPAA)*. IEEE, 2023, pp. 1–5.
- [52] Q. Tang, N. Sang, and T. Zhang, "Extraction of salient contours from cluttered scenes," *Pattern recognition*, vol. 40, no. 11, pp. 3100–3109, 2007.
- [53] P. J. Burt and E. H. Adelson, "The laplacian pyramid as a compact image code," in *Readings in computer vision*. Elsevier, 1987, pp. 671–679.
- [54] J. Peeples, S. A. Kharsa, L. Saleh, and A. Zare, "Histogram layers for neural engineered features," *arXiv preprint arXiv:2403.17176*, 2024.
- [55] C.-Y. Yeh, Y.-C. Liu, D.-A. Huang, and J.-B. Huang, "Equivariant wasserstein knowledge distillation," in *Proceedings of the IEEE/CVF Conference on Computer Vision and Pattern Recognition*, 2021, pp. 14 616–14 625.
- [56] A. Kendall, Y. Gal, and R. Cipolla, "Multi-task learning using uncertainty to weigh losses for scene geometry and semantics," in *Proceedings of the IEEE conference on computer vision and pattern recognition*, 2018, pp. 7482–7491.
- [57] M. Irfan, Z. Jiangbin, S. Ali, M. Iqbal, Z. Masood, and U. Hamid, "Deepship: An underwater acoustic benchmark dataset and a separable convolution based autoencoder for classification," *Expert Systems with Applications*, vol. 183, p. 115270, 2021.
- [58] S. S. Nathala, R. R. Yakkati, A. Dayal, M. S. Manikandan, J. Zhou, and L. R. Cenkeramaddi, "Vessel type classification utilizing underwater acoustic data and deep learning," in *2024 IEEE 19th Conference on Industrial Electronics and Applications (ICIEA)*. IEEE, 2024, pp. 1–6.
- [59] D. S. Park, W. Chan, Y. Zhang, C.-C. Chiu, B. Zoph, E. D. Cubuk, and Q. V. Le, "SpecAugment: A simple data augmentation method for automatic speech recognition," *arXiv preprint arXiv:1904.08779*, 2019.
- [60] Q. Kong, Y. Cao, T. Iqbal, Y. Wang, W. Wang, and M. D. Plumbley, "Panns: Large-scale pretrained audio neural networks for audio pattern recognition," *IEEE/ACM Transactions on Audio, Speech, and Language Processing*, vol. 28, pp. 2880–2894, 2020.
- [61] A. Baevski, H. Zhou, A. Mohamed, and M. Auli, "wav2vec 2.0: A framework for self-supervised learning of speech representations," in *Advances in Neural Information Processing Systems*, vol. 33, 2020, pp. 12 449–12 460.
- [62] W.-N. Hsu, B. Bolte, Y.-H. H. Tsai, K. Lakhotia, R. Salakhutdinov, and A. Mohamed, "Hubert: Self-supervised speech representation learning by masked prediction of hidden units," *IEEE/ACM Transactions on Audio, Speech, and Language Processing*, vol. 29, pp. 3451–3460, 2021.
- [63] A. Radford, J. W. Kim, T. Xu, G. Brockman, C. McLevey, and I. Sutskever, "Robust speech recognition via large-scale weak supervision," *arXiv preprint arXiv:2212.04356*, 2022.
- [64] J. F. Gemmeke, D. P. Ellis, D. Freedman, A. Jansen, W. Lawrence, R. C. Moore, M. Plakal, and M. Ritter, "Audio set: An ontology and human-labeled dataset for audio events," in *2017 IEEE international conference on acoustics, speech and signal processing (ICASSP)*. IEEE, 2017, pp. 776–780.
- [65] A. Mohammadi, T. Kelhe, D. Carreiro, A. Van Dine, and J. Peeples, "Cross-domain knowledge transfer for underwater acoustic classification using pre-trained models," *arXiv preprint arXiv:2409.13878*, 2024.
- [66] J. Yang, X. Zhu, A. Bulat, B. Martinez, and G. Tzimiropoulos, "Knowledge distillation meets open-set semi-supervised learning," *International Journal of Computer Vision*, pp. 1–20, 2024.
- [67] L. Yuan, F. E. Tay, G. Li, T. Wang, and J. Feng, "Revisiting knowledge distillation via label smoothing regularization," in *Proceedings of the IEEE/CVF conference on computer vision and pattern recognition*, 2020, pp. 3903–3911.
- [68] Y. Tian, D. Krishnan, and P. Isola, "Contrastive representation distillation," in *International Conference on Learning Representations*.
- [69] Y. Zhang, X. Lan, Y. Dai, F. Zeng, Y. Bai, J. Chang, and Y. Wei, "Prime-aware adaptive distillation," in *Computer Vision—ECCV 2020: 16th European Conference, Glasgow, UK, August 23–28, 2020, Proceedings, Part XIX 16*. Springer, 2020, pp. 658–674.
- [70] B. Peng, X. Jin, J. Liu, D. Li, Y. Wu, Y. Liu, S. Zhou, and Z. Zhang, "Correlation congruence for knowledge distillation," in *Proceedings of the IEEE/CVF International Conference on Computer Vision*, 2019, pp. 5007–5016.
- [71] Y. Matsubara, "torchdistill: A modular, configuration-driven framework for knowledge distillation," in *International Workshop on Reproducible Research in Pattern Recognition*. Springer, 2021, pp. 24–44.
- [72] L. Gao and H. Gao, "Feature decoupled knowledge distillation via spatial pyramid pooling," in *Proceedings of the Asian Conference on Computer Vision*, 2022, pp. 1109–1123.
- [73] C. Chen, J. Zhang, Y. Xu, L. Chen, J. Duan, Y. Chen, S. Tran, B. Zeng, and T. Chilimbi, "Why do we need large batchsizes in contrastive learning? a gradient-bias perspective," *Advances in Neural Information Processing Systems*, vol. 35, pp. 33 860–33 875, 2022.
- [74] P. Lu, A. Ghaddar, A. Rashid, M. Rezagholizadeh, A. Ghodsi, and P. Langlais, "Rw-kd: Sample-wise loss terms re-weighting for knowledge distillation," in *Findings of the Association for Computational Linguistics: EMNLP 2021*, 2021, pp. 3145–3152.
- [75] A. Psaltis, C. Chatzikonstantinou, C. Z. Patrikakis, and P. Daras, "Fedrcil: Federated knowledge distillation for representation based contrastive incremental learning," in *Proceedings of the IEEE/CVF International Conference on Computer Vision*, 2023, pp. 3463–3472.